

# Bragg coherent diffractive imaging of strain at the nanoscale

Cite as: J. Appl. Phys. **125**, 121101 (2019); doi: [10.1063/1.5054294](https://doi.org/10.1063/1.5054294)

Submitted: 30 August 2018 · Accepted: 7 March 2019 ·

Published Online: 28 March 2019



Dmitry Karpov<sup>1,a)</sup> and Edwin Fohtung<sup>1,2,b)</sup>

## AFFILIATIONS

<sup>1</sup>Department of Physics, New Mexico State University, Las Cruces, New Mexico, 88003, USA

<sup>2</sup>Associate Laboratory Directorate for Physical Science (ALDPS), Los Alamos National Laboratory, Los Alamos, New Mexico, 87545, USA

**Note:** This paper is part of the Special Topic section “Strain engineering in functional materials,” J. Appl. Phys. 125(8) (2019).

**a) Present address:** Paul Scherrer Institute, Swiss Light Source, 5232 PSI-Villigen, Switzerland.

**b) Author to whom correspondence should be addressed:** [efohtung@nmsu.edu](mailto:efohtung@nmsu.edu)

## ABSTRACT

Strain engineering is a promising technology with potential application in memory devices, electronic elements, photoactive materials, etc. Nanoscale imaging of the strain is therefore important to better understand the operating condition of the device, growth processes, and influences of other factors. X-rays offer the advantage over electron-based techniques in that they offer high spatial resolution and access to volumetric information within nanostructured materials. This paper describes the basic physics behind strain at the nanoscale and provides a concise summary of the efforts in coherent diffractive imaging for the imaging of the displacement fields in nanocrystals. Although the approach is still under development, with instruments being continuously improved, a number of important results have already been demonstrated.

Published under license by AIP Publishing. <https://doi.org/10.1063/1.5054294>

## I. INTRODUCTION

Tuning the strain parameter in nanostructures has been extensively researched for possible enhancement of carrier mobility, emergent multiferroic properties, superconductivity, tuning of bandgap and the Curie temperature, and many other functional properties. The examples of strain engineering applications range from metal oxide semiconductor field-effect transistor (MOSFET) devices to various functional complex oxides.<sup>1,2</sup> The mechanisms of strain relaxation and dislocation dynamics in nanoscale materials are still not fully understood. To carry out quantitative and qualitative studies, one needs a tool with high spatial resolution and strain sensitivity as well as penetrability through hundreds of atomic layers. While electron imaging methods<sup>3,4</sup> provide unbeatable surface spatial resolution, they have limited penetrability of a few nanometers, and since the electron beam also interacts with an external electric and magnetic field, their application for volumetric and dynamical strain mapping in the volume of nanostructures and heterostructures is greatly hindered. The atom probe tomography (APT) technique can access the information beyond a single cubic nanometer,<sup>5</sup> but one must accept the destruction of the

sample in the process. These limitations can be surpassed through the use of coherent X-ray imaging techniques. These techniques enjoyed fast development in the last few decades alongside advancements in third and fourth generation synchrotron radiation facilities<sup>6–8</sup> and dedicated focusing X-ray optics.<sup>9–11</sup> Modern synchrotron beamlines produce a spatially and temporally coherent X-ray flux of  $10^8$  photons per second that can be focused down to 10 nm,<sup>12</sup> providing the possibility to resolve the structure of materials with high-resolution using probing techniques such as scanning X-ray diffraction mapping<sup>13</sup> and Bragg coherent diffractive imaging (BCDI).<sup>14–17</sup> Especially noticeable is the ability of such techniques to resolve volumetric strain distribution and evolution in individual and extended nanostructures. In scanning X-ray diffraction mapping, the resolution is “beam size” limited,<sup>18,19</sup> while BCDI can provide information about the nanocrystals internal strain, shape, and response functions such as electric polarization<sup>17</sup> with high spatial resolution<sup>20</sup> limited only by the wavelength of X-rays and angular acceptance of the detector.

In this tutorial article, we will first address the X-ray Bragg coherent diffractive imaging technique, which has found applications in recent years<sup>14–17</sup> as a primary tool to map volumetric

nanoscale strains in studies of samples ranging from semiconductor to metallic and oxide nanostructures. Next, we shall proceed into the methodology behind coherent diffractive imaging, which is based on the iterative reconstruction of lost information of the scattered X-ray wavefront. We also briefly discuss the specifics of coherent X-ray scattering by strained crystals and typical schemes of a modern Bragg coherent diffractive imaging experiment. This is followed by a few examples of strain imaging. We take a look at strain fields (i) within a transition metal, (ii) a semiconductor, and (iii) a perovskite crystal. In the end, we offer a discussion on the method's current achievements and potential future developments.

## II. ELASTICITY

### A. Fundamentals of elasticity theory

Elasticity is the property of a physical body to undergo deformation upon application of external loads and regain its initial shape after these loads have been removed. The three most important concepts of the elasticity theory are *stress*, *strain*, and *displacement fields*. The elasticity is typically considered within the linear limit (when stress-strain relation is linear) and beyond the linear limit that is beyond the scope of this tutorial. Stress can be understood as a tensorial force within every volumetric element of the material (see Fig. 1), as a result of both external and internal thermodynamical influences. Stress can be compressive, tensile, shear, or a combination of them (not in a single volume element, but rather in a local cluster). Application of stress on the material results in the material being deformed. The emanating deformation field can be characterized by the strain tensor. In materials systems, strain can be homogenous, heterogeneous, or inhomogeneous.

Classical mechanics of deformations within solid state physics is a broad topic beyond the scope of our paper. However, we will outline fundamental concepts and relationships within the elasticity theory, important in the framework of Bragg coherent diffractive imaging. The relationship between the strain tensor  $\epsilon$  and the

displacement field  $\mathbf{u}$  for a linear isotropic medium is given by<sup>21</sup>

$$\epsilon_{ij} = \frac{1}{2} \left( \frac{\partial u_i}{\partial x_j} + \frac{\partial u_j}{\partial x_i} \right), \quad i, j = 1, 2, 3. \quad (1)$$

Stress at equilibrium can be described by the equilibrium equations

$$\frac{\partial \sigma_{11}}{\partial x_1} + \frac{\partial \sigma_{12}}{\partial x_2} + \frac{\partial \sigma_{13}}{\partial x_3} = 0, \quad (2)$$

$$\frac{\partial \sigma_{21}}{\partial x_1} + \frac{\partial \sigma_{22}}{\partial x_2} + \frac{\partial \sigma_{23}}{\partial x_3} = 0, \quad (3)$$

$$\frac{\partial \sigma_{31}}{\partial x_1} + \frac{\partial \sigma_{32}}{\partial x_2} + \frac{\partial \sigma_{33}}{\partial x_3} = 0. \quad (4)$$

Constitutive equations describe the relationship between the stress and the strain. There are two alternative ways to write Hooke's law

$$\sigma_{ij} = C_{ijkl} \epsilon_{kl}, \quad (5)$$

$$\epsilon_{ij} = S_{ijkl} \sigma_{kl}, \quad (6)$$

where  $C_{ijkl}$  and  $S_{ijkl}$  are the stiffness coefficient and compliance coefficient tensors, respectively.

The ability of engineering elastic strain of materials at the nano- and mesoscale has attracted a lot of attention in the materials science community. Advanced actuators capable of exerting enhanced stress fields in materials are needed.<sup>22,23</sup> The changes of interatomic distances between constitutive atoms [see Eq. (1)] in a material, known as the strain or mechanical deformation, create a displacement field  $\mathbf{u}$  that affects most of the physical properties of the materials. The strain tensor [see Eqs. (1) and (6)] describes the deformation of an element of the material. The strain tensor contains six independent components ( $\epsilon_{xx}$ ,  $\epsilon_{yy}$ ,  $\epsilon_{zz}$ ,  $\epsilon_{xy}$ ,  $\epsilon_{xz}$ ,  $\epsilon_{yz}$ ), which are related to the stress components by the compliance tensor of the material (in the linear regime). The ability to reshape the displacement field is at the heart of strain engineering by essentially exploiting the tensorial character of the strain field.<sup>24</sup>

Piezoelectric actuators are suitable for transferring strain fields to attached films containing embedded active nanomaterials, where the maximum achievable tuning of their properties is eventually conditioned by the elastic limit of the material ( $\sim 1\%$  in most bulky solid-state structures). Molecular beam epitaxy of ferroelectrics such as BaTiO<sub>3</sub> films on Si, Ge, and GaAs substrates have been successfully applied to engineer strain for a variety of applications.<sup>25</sup> Nanometric and low-dimensional materials have been reported to show unusual mechanical responses where the elastic limit scales up as the inverse of a dominant characteristic length related to the size of the material.<sup>26</sup> Moreover, in the limit of thin monolayers, the so-called two-dimensional (2D) materials feature unprecedented high "stretchability" up to  $\sim 20\%$  of strain magnitudes (before breakdown), providing a large playground for strain engineering. The ability to spatially resolve and map strains at the nanoscale in semiconductors, complex oxides, and most functional oxides are essential to strain engineering and device fabrications.

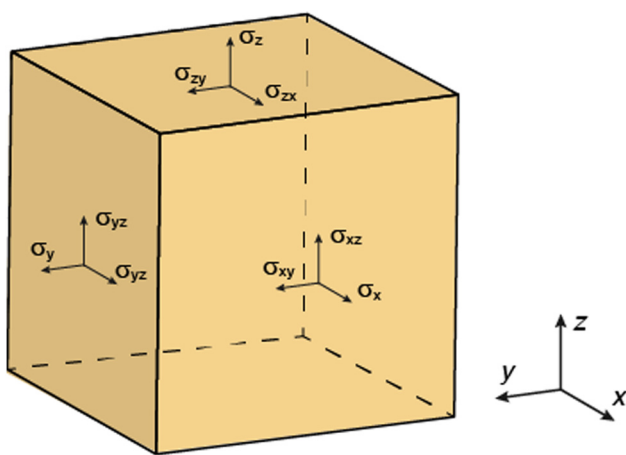
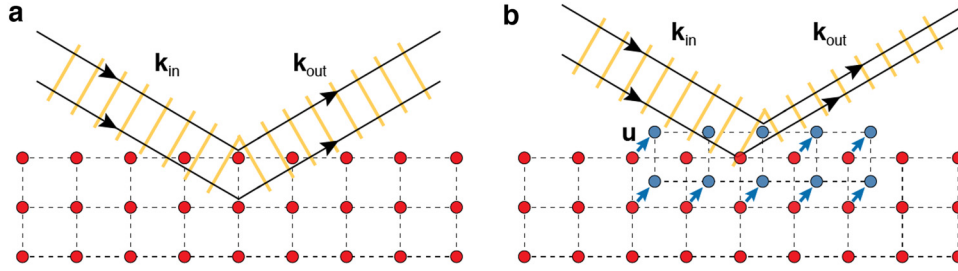


FIG. 1. Geometry of the stress tensor.



**FIG. 2.** Relationship between the atomic displacement field, d-spacing, and the wavevector. (a) Unstrained crystal and (b) strained crystal.

### III. COHERENT DIFFRACTIVE IMAGING

#### A. X-ray scattering by a strained crystal

The physical structure of materials is responsible for the different properties that these materials possess. Understanding structure-property relationships is one of the primary tasks of modern material science. The scattering of X-ray radiation from a sample region allows access to the electron density distribution, lattice spacing within crystals, materials composition, and other structural information.

The Bragg coherent diffractive imaging is among the novel techniques where information from individual nanostructures is available to the experimenter. This shift of paradigm from studies of common structural signatures in ensembles of nanostructures to the imaging of individual goes together with the development of manufacturing techniques, where the quest for miniaturization has led far beyond sub-micrometer scales.<sup>27</sup>

The characterization of nanoscale materials requires X-rays with coherence larger than the volume of the nanostructure under study. The coherent volume is defined by the spatial and temporal coherence lengths. Photon emission in radiation sources shows different degree of spontaneity, resulting in various degree of correlation between wavefronts at different coordinate points (spatial coherence) and at different moments in time (temporal coherence). To increase the degree of spatial coherence, filters such as pinholes and slits are introduced in the beam while monochromators improve temporal coherence.

Given a coherent X-ray beam, radiation amplitude,  $A(\mathbf{q})$ , elastically scattered [see Fig. 2(a)] from a crystal can be written as<sup>28,29</sup>

$$A(\mathbf{q}) = \int \rho(\mathbf{r}) e^{-i\mathbf{q} \cdot \mathbf{r}} d\mathbf{r}. \quad (7)$$

In this expression, we assume kinematical scattering and the first Born approximations, and  $\mathbf{r}$  indicates the radius vector to the detector plane where the diffraction patterns (see Fig. 3) are recorded,  $\mathbf{q} = \mathbf{k}_{\text{out}} - \mathbf{k}_{\text{in}}$  is the moment transfer vector and  $\rho(\mathbf{r})$  is the real-valued electron density distribution. For an unstrained crystal, the electron density can be expressed through shape function  $s(\mathbf{r})$  and Bravais lattice  $\mathbf{R}_m$ ,

$$\rho(\mathbf{r}) = s(\mathbf{r}) \sum_m \delta(\mathbf{r} - \mathbf{R}_m). \quad (8)$$

For a strained crystal, a vector strain field  $\mathbf{u}(\mathbf{R}_m)$  needs to be considered, resulting in new expression for electron density  $\tilde{\rho}(\mathbf{r}) = s(\mathbf{r}) \sum_m \delta[\mathbf{r} - \mathbf{R}_m - \mathbf{u}(\mathbf{R}_m)]$ , and the corresponding amplitude

distribution

$$A(\mathbf{q}) = \int \tilde{\rho}(\mathbf{r}) e^{-i\mathbf{q} \cdot \mathbf{r}} d\mathbf{r} = S(\mathbf{q}) * F(\mathbf{q}) \sum_m e^{i\mathbf{q} \cdot [\mathbf{R}_m + \mathbf{u}(\mathbf{R}_m)]}, \quad (9)$$

where  $S(\mathbf{q})$  is the Fourier transform of the shape function and  $F(\mathbf{q})$  is the normalized structure factor. Equation (9) can be simplified if we consider only the region in the vicinity of a Bragg peak  $\mathbf{G}_0$  and small magnitudes of vector strain field  $\mathbf{u}(\mathbf{R}_m)$ <sup>30</sup>

$$A(\mathbf{q}) = S(\mathbf{q}) * F(\mathbf{q}) \sum_m e^{i\mathbf{q} \cdot \mathbf{R}_m [1 + i\mathbf{G}_0 \cdot \mathbf{u}(\mathbf{R}_m)]}. \quad (10)$$

With these approximations, the crystal is understood to be elastically strained and the structure factor undistorted.<sup>31</sup> Finally, we can wrap up a compact equation for the scattered amplitude

$$A(\mathbf{q}) = \int \rho(\mathbf{r}) e^{-i\mathbf{G}_0 \cdot \mathbf{u}(\mathbf{r})} e^{-i\mathbf{q} \cdot \mathbf{r}} d\mathbf{r} = \int \rho(\mathbf{r}) e^{-i\phi(\mathbf{r})} e^{-i\mathbf{q} \cdot \mathbf{r}} d\mathbf{r}. \quad (11)$$

With Eq. (11), we can describe a strained crystal in terms of the complex-valued electron density with phase part  $\phi(\mathbf{r})$  encoding the strain vector field projected on  $\mathbf{G}_0$  [Fig. 2(b)]. If the illuminating beam is coherent, and the measured diffraction pattern is sampled at the Nyquist frequency, then the lost phase can be retrieved from the measured intensity in the reciprocal space. The resolution of the reconstructed images is only limited by the wavelength of X-rays and the angular acceptance of the detector. It is important to note that for highly strained crystals the kinematic theory cannot always provide adequate results and dynamical approach generalized by Takagi and Taupin<sup>32–34</sup> should be applied.

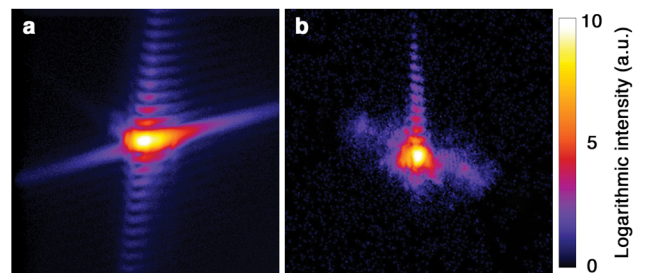


**FIG. 3.** X-ray diffraction patterns of a single Bragg peak of (a) homogeneously and (b) inhomogeneously strained nanocrystal.

A detailed overview of the dynamical diffraction theory is given in a number of works.<sup>35,36</sup>

One particularly useful property of the diffraction is that simply looking at the visual symmetry allows one to predict the presence of strain. As it was noted in Ref. 35, unstrained crystals exhibit centro-symmetric 3D diffraction [Fig. 3(a)] patterns, while displacement introduces phase shifts resulting in stronger visual asymmetry of the reciprocal Bragg peak [Fig. 3(b)]. Reconstruction of the full strain tensor from strain vector fields shown in Eq. (1) became recently possible due to improvements in stability of the instrumental stations dedicated to BCDI.<sup>37</sup> However, the application of the technique to systems beyond elastic limits yet is challenging and requires additional modelling.

## B. Phase problem

The advantage of X-ray techniques over alternative nanoscale imaging methods is reduced by the challenges in dedicated optics fabrication. This challenge forced the X-ray community to approach X-ray microscopes designs differently from optical analogies. Modern detectors of X-ray radiation are not capable of recording high-resolution wavefront information. The interferometric approach allows recording of the phase but is currently limited by manufacturing precision of X-ray gratings. This inability to record the high-resolution phase is called the phase problem. Given both phase and amplitude information are available, one can simply inverse Fourier transform the diffraction pattern and obtain real space image of the sample with high resolution, effectively performing computational image formation instead of optical. Importance of the phase information can be illustrated by swapping phases of two images in their Fourier transform (see Fig. 4).

To bypass the phase problem, a number of algorithmic approaches emerged that attempt to iteratively reconstruct missing phase information. These approaches are largely based on the initial observation of Sayre<sup>39</sup> regarding the sampling requirements for direct structure determination. Series of algorithms for phase retrieval rely on the idea that if a finite support of the object in the

real space and partial information on the Fourier transform of the object in the reciprocal space are available then the phase information can be retrieved. The groundwork was done by Fienup which resulted in the development of error-reduction and input-output algorithms.<sup>40</sup> The oversampling requirements are discussed in detail in the work by Miao *et al.*<sup>41</sup>

## C. Iterative phase retrieval

A number of phase retrieval algorithms have been developed to date. Detailed review can be found in Ref. 42. Arguably, among the most important ones are the error reduction (ER) and hybrid input-output (HIO).<sup>40</sup> The ER algorithm is a modification of an algorithm proposed by Gerchberg and Saxton (GS)<sup>43</sup> for electron diffraction. The principal scheme of a prototypical iterative phase retrieval is shown in Fig. 5. In the GS algorithm, the reconstruction process starts with assigning a random set of phases to the measured diffraction amplitudes  $\tilde{\varphi}_0(\mathbf{q})$  in the reciprocal space to form a complex-valued *modified amplitude*

$$\tilde{E}_0(\mathbf{q}) = \sqrt{I(\mathbf{q})} \cdot \exp[i \tilde{\varphi}_0(\mathbf{q})]. \quad (12)$$

This *modified amplitude pattern* is then inverse Fourier transformed into the real space to form a *modified object*. A number of constraints can be applied to the object in the real space, one of which is the finite support  $\Xi(\mathbf{r})$  that represents an area where the electron density of a sample has non-zero values. After the application of the known constraints, the object is Fourier transformed and new complex-valued diffraction amplitude is generated. At this step, the magnitude of the new diffraction amplitude is replaced by the experimentally measured one and the whole procedure of projecting between real and reciprocal space is repeated until the solution is found

$$\tilde{E}_n(\mathbf{q}) = |\tilde{E}_n(\mathbf{q})| \cdot \exp[i \tilde{\varphi}_n(\mathbf{q})] = \mathcal{F}\{E_n(\mathbf{r})\}, \quad (13)$$

$$\tilde{E}'_n(\mathbf{q}) = \sqrt{I(\mathbf{q})} \cdot \exp[i \tilde{\varphi}_n(\mathbf{q})], \quad (14)$$

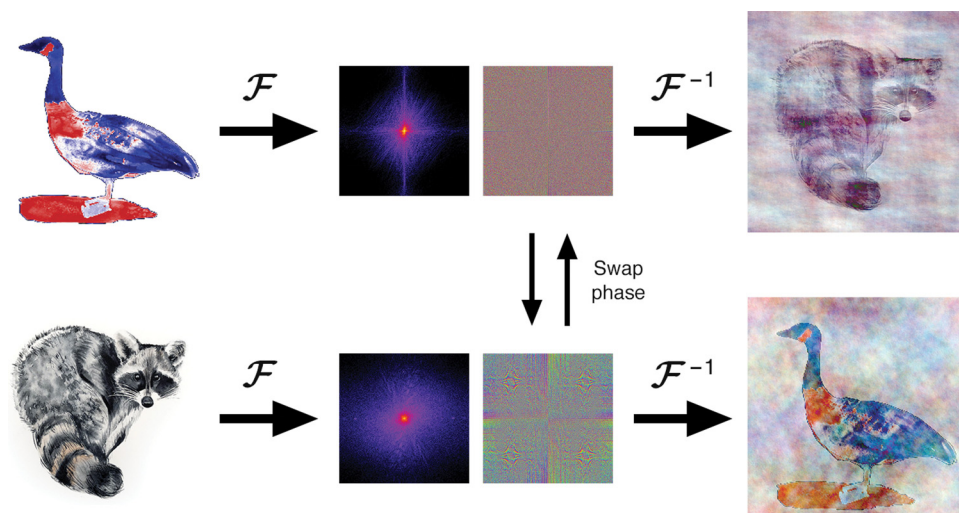


**FIG. 4.** Importance of the phase information in the Fourier space. The swapping phases of images in the Fourier domain results in swapping of spatial distribution of the signal in the real space. This suggests that the phase plays an important part in encoding the underlying structure of images and is essential for their reconstruction.



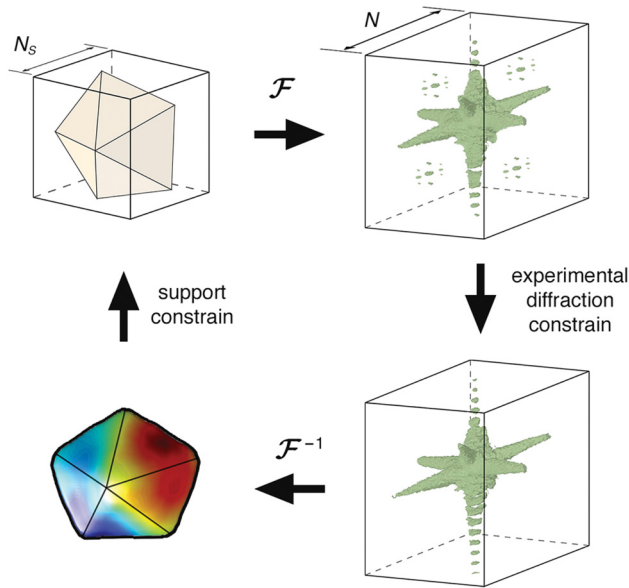


**FIG. 5.** Iterative phase retrieval scheme. The experimentally measured amplitude pattern is updated with random phases and then inverse Fourier transformed. Known constraints, such as shape, are applied on the resulted complex-valued object which then forward Fourier transformed to obtain a new complex-valued diffraction amplitude. The magnitude of the pattern at this step is replaced by the experimentally recorded amplitude and the process is repeated until the final solution is found.

$$E'_n(\mathbf{r}) = |E'_n(\mathbf{r})| \exp[i\phi'_n(\mathbf{r})] = \mathcal{F}^{-1}\{\tilde{E}'_n(\mathbf{q})\}, \quad (15)$$

$$E_{n+1}(\mathbf{r}) = \Xi(\mathbf{r}) \exp[i\phi_{n+1}(\mathbf{r})] = \Xi(\mathbf{r}) \exp[i\phi'_n(\mathbf{r})]. \quad (16)$$

One can see that phase retrieval is an optimization problem where the task is to find a solution with a minimum error between the calculated and experimentally measured diffraction magnitudes. This algorithm was generalized and called ER by Fienup for the cases where only partial knowledge on the sample can be used, but where the positivity constraint can be assumed.<sup>40</sup> Both of these algorithms minimize the error on each iteration. This property often leads them to stagnation in the local minimal error of the reconstruction preventing from convergence to the true solution.

Fienup has developed another algorithm that has a higher success rate in overcoming this stagnation problem. The HIO algorithms<sup>40</sup> use a combination between the solutions on current and previous steps that is driven by feedback parameter  $\beta$  that is usually chosen between 0.5 and 1. The iterative scheme is designed such that after a minimal error has been achieved and the algorithm stagnates, the positive feedback accumulates forcing the current solution to leave from the local minimum and search further. The operations in the Fourier space are identical to the ER algorithm, while in the real space, the steps can be formulated as follows:

$$E_{n+1}(\mathbf{r}) = \begin{cases} E'_n(\mathbf{r}), & \mathbf{r} \notin \Xi', \\ E_n(\mathbf{r}) - \beta E'_n(\mathbf{r}), & \mathbf{r} \in \Xi'. \end{cases} \quad (17)$$

It is worth mentioning that there exists another class of algorithms for the phase retrieval which is based on the gradient descent optimization algorithm.<sup>40,44</sup> There has been less effort to use this class of algorithms in BCDI due to a number of reasons. One of the major reasons is that the less computationally demanding algorithms such as steepest descent<sup>40,44</sup> and conjugate gradient<sup>44,45</sup> are not showing substantial benefits over HIO-ER combination, neither in terms of convergence or speed. Another exemplary algorithm of the class is the Broyden-Fletcher-Goldfarb-Shanno (BFGS) algorithm,<sup>46</sup> which is unfortunately greedy for the computational resources and shows slower convergence in general. However, with the current growth of computational power one might explore this class of algorithms for the problems of nanoscale imaging.

#### D. Bragg coherent diffractive imaging

The Bragg coherent diffractive imaging technique relies on the high coherence of synchrotron and X-ray free electron laser beams. This method of exploiting coherence to the probe strain inside small crystals has been developed for over a decade now.<sup>14–17,38,47</sup> A major breakthrough was achieved by the group of Robinson that demonstrated inversion of three-dimensional diffraction near the Bragg point into a real-space volume of the gold nanocrystal.<sup>15</sup> Figure 6 shows slices of the reconstructed particle made more than a decade ago. In the recent years, the X-ray Bragg coherent diffractive imaging has enjoyed a number of successful applications to challenging problems in materials science ranging from the formation of dislocations<sup>48</sup> and ultrafast lattice dynamics in individual nanocrystals<sup>49</sup> to imaging of topological defects in ferroelectric materials<sup>17</sup> and battery structures.<sup>50</sup>

The importance of the studies of both hard and soft condensed matter at the nanoscale hardly deserves a debate due to the role nanotechnology has already played in the establishment of modern electronics, catalysis materials, energy harvesting materials, and many other fields. It is worth, however, mentioning why full volume studies of systems in dynamics or *in operando* presented in works<sup>17,48–50</sup> are of interest right now. Lattice dynamics<sup>49</sup> is one of the key processes influencing transitions in condensed matter and their influence on various properties of nanomaterials features many theoretical models in need of experimental data for further understanding and refinement. It is especially important to have access to the volume of nanocrystals, where a magnitude of secondary effects can be generated or suppressed. Another object of interest for crystallographers for many years is dislocations in crystals and their propagation in crystals under the external influence that was addressed in work.<sup>48</sup> Dislocations are volumetric entities and so require penetrating probes like X-rays while at the same time demand nanoscale resolution to be observed. Both properties are conveniently offered by the BCDI technique. The other two examples<sup>17,50</sup> show the application cases of the technique to the imaging of processes that are going on in functional materials when the geometry (size and shape relation) and the energy landscape are favorable for the formation of topological defects.

Usually in the Bragg coherent diffractive imaging, the diffraction pattern of a nanocrystal, once coherently illuminated, contains interference from all the sample regions appearing as fringe

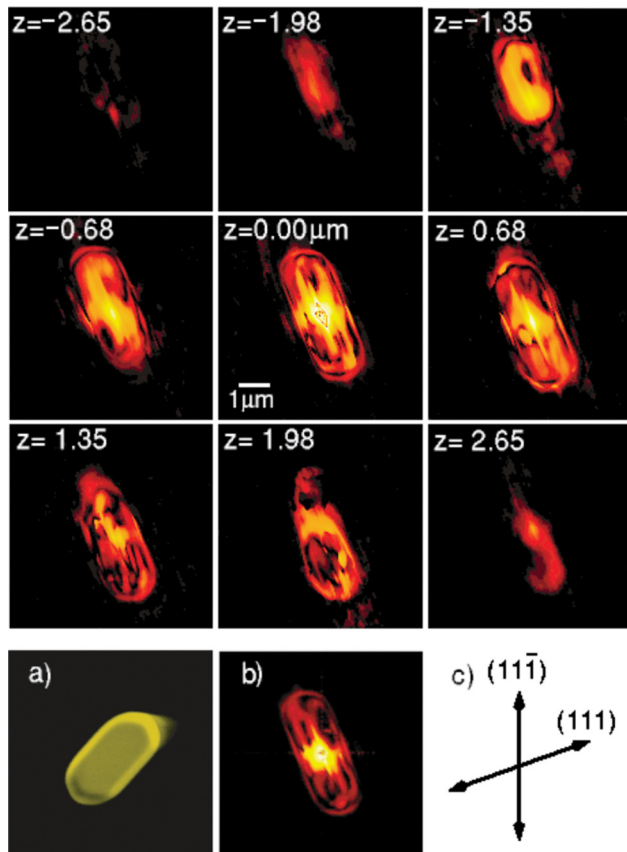


**FIG. 6.** Top panels show slices through the reconstructed volume of the Au nanoparticle. Bottom panels show (a) the SEM image of the nanoparticle, (b) Middle slice through the volume, (c) Coordinate system. Reprinted with permission from Williams *et al.* Phys. Rev. Lett. **90**, 175501 (2003).<sup>15</sup> Copyright 2003 American Physical Society.

oscillations in the vicinity of each Bragg peak in 3D. The most trivial fringe types are those arising from interference between opposing facets on the crystal shape. This simplistic diffraction manifests itself as a “sinc” function with a fringe spacing on the detector  $t$  given by the *grating formula*,

$$t = \lambda D/d, \quad (18)$$

where  $\lambda$  is the wavelength of incident coherent x-rays,  $d$  is the distance between the facets (i.e. the size of the sample), and  $D$  is the distance to the detector.

The shape of the nanocrystal and the local strain are always encoded in the Bragg peak. If the crystal has a spherical shape, the diffraction pattern will have circular symmetry described by a corresponding 3D Airy function, while a faceted crystal will give a combination of both of these patterns as an amplitude superposition.

The typical experimental scheme for the Bragg coherent diffractive imaging technique is shown in Fig. 7. The sample is placed on top of a goniometer, allowing fine adjustment of roll and pitch to manipulate the footprint size of the incident beam. A stepping stage allows the positioning of the sample in rectangular coordinates along the  $x$ ,  $y$ , and  $z$  directions. The rocking of the sample is done with a high precision rotation stage. The detector is fit to a motorized positioning system and moves in spherical coordinates around the sample. The detector can also be moved to and from the sample to magnify the diffraction pattern. Notable synchrotron stations for conducting BCDI measurements are ID-34-C of Advanced Photon Source,<sup>51</sup> I13 of the Diamond Light Source,<sup>52</sup> ID01 at the European Synchrotron Radiation Facility,<sup>53</sup> P10 at PETRA III,<sup>54</sup> and recently NanoMAX at MAX IV.<sup>55</sup>

Such experiments usually start with an unfocused X-ray beam to locate crystallographic reflections on the powder ring. To reconstruct the strain tensor of nanomaterials (see Fig. 8), it is important to record high-resolution diffraction at multiple Bragg points.<sup>37,56</sup> In principle, three linearly independent reflections from

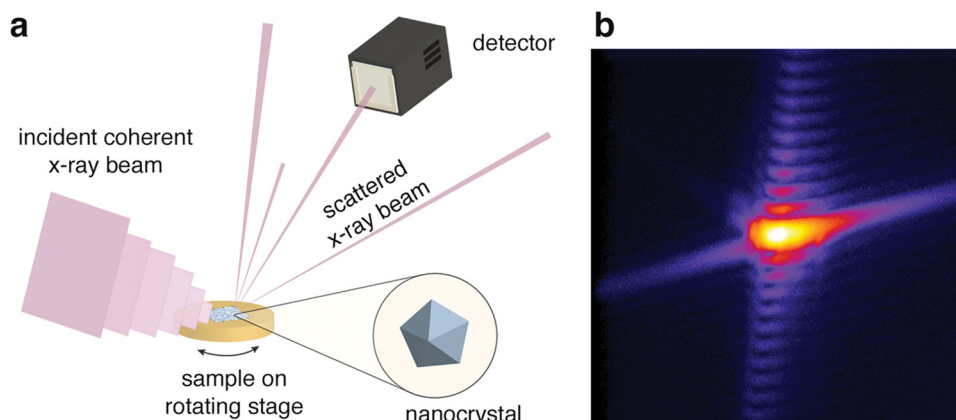


**FIG. 7.** Bragg coherent diffraction experiment. (a) Typical experimental scheme with plane X-ray wave being scattered by the sample crystal planes into corresponding Bragg angles. (b) Diffraction pattern of an individual Bragg reflection recorded by a pixelated detector.

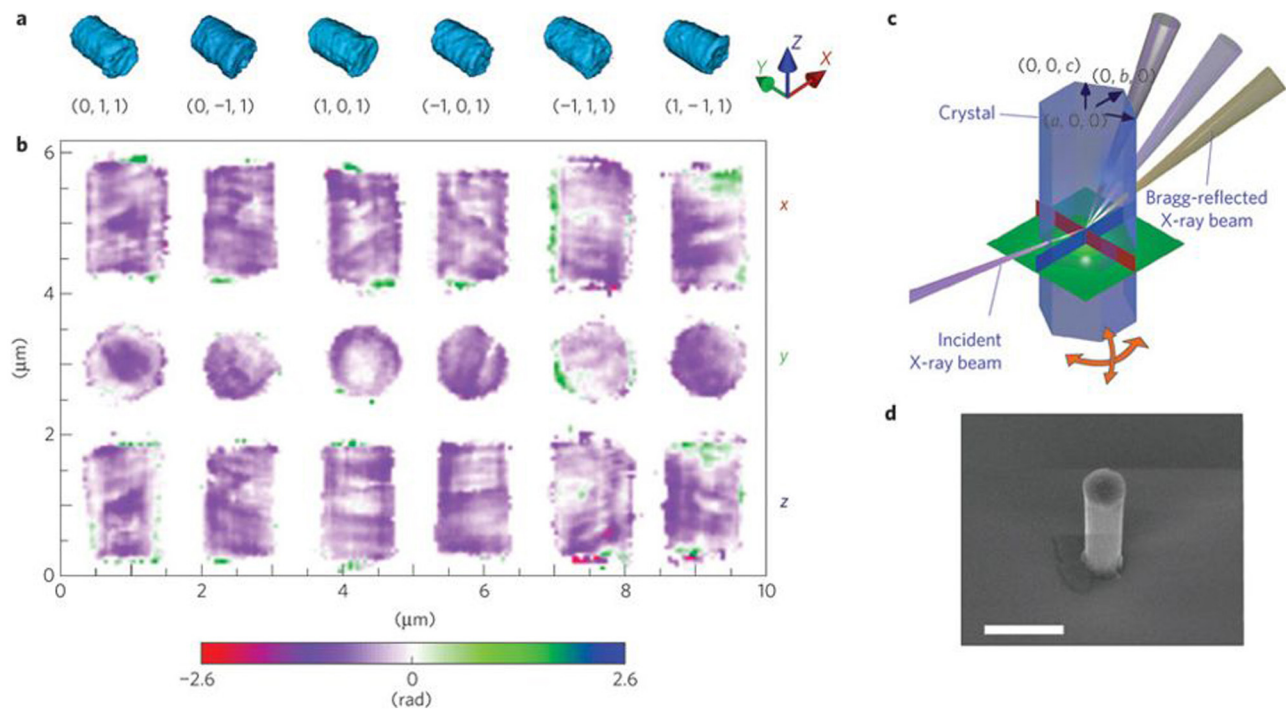


**FIG. 8.** Amplitudes (a) and phases (b) reconstructed from 6 different Bragg reflections of the individual ZnO nanorod (d). The experimental geometry is shown in (c). Reprinted with permission from Newton *et al.* Nat. Mater. **9**, 120–124 (2010).<sup>37</sup> Copyright 2009 Nature Publishing Group.

orthogonal crystal planes are sufficient to recover the displacement vector, but this requirement can be relaxed to 2 reflections.<sup>37</sup> However, many for many applications of the technique a single reflection is sufficient and allows to conduct dynamic experiments.<sup>17,49,50</sup> When the reflections identified, a series of focusing is performed so that a single nanoparticle is illuminated with the X-ray beam. After that, the detector is positioned at a distance where a selected Bragg reflection is sufficiently sampled by a pixelated detector. The sample is then rocked by a small angle with the stepping of<sup>57</sup>

$$\Delta\theta < \lambda/(4D \sin \theta_{\text{Bragg}}), \quad (19)$$

where  $\lambda$  is the wavelength of incident X-ray radiation,  $D$  is the size of scattering feature, and  $\theta_{\text{Bragg}}$  is the Bragg scattering angle. Adjusting the angle by a step below  $\Delta\theta$  allows one to satisfy the Shannon sampling condition of  $\pi/D$ . Rocking of the sample allows visualization of the three-dimensional diffraction intensity that contains information on the sample in real-space. If the measured diffraction pattern is properly sampled it can be reconstructed to obtain real space complex density  $\tilde{\rho}(\mathbf{r})$  using a suitable phase retrieval algorithm. Traditionally, for Bragg coherent diffractive imaging, the most important algorithm is Fienup's *Hybrid Input-Output* (HIO) method, which helps to avoid stagnation problems.<sup>40</sup>

## IV. EXAMPLES OF STRAIN IMAGING

### A. Transition metal

Transition metal nanomaterials are predicted to have a broad range of applications as sensor elements, catalysis, magnetic systems, energy storage, and many others. Moreover, dual systems, such as “core-shell,” are in the spotlight of researchers since they have an even a greater degree of tunability, better working conditions through protection of the core layer by the shell layer and better separation of multiple nanostructures, as well as possible interface effects.

Altering the growth conditions of dual-system nanomaterials can lead to strain fields and defect networks. Such crystallographic imperfections change the properties of the nanomaterials and motivate researchers to develop tools for their investigation. Coherent imaging methods are convenient because they can be implemented along with the growth chambers for *in situ* studies.

As an example, we show results from the imaging of an individual nickel nanowire (NW).<sup>47</sup> The nanowires were grown on the Si substrate using a chemical vapor deposition method at 650°C. The crystallinity of the nanowires was confirmed with electron diffraction, while SEM micrographs provided knowledge on the shape. Growth information suggested surface impurities in the nanowires. *A priori* information on the shape, crystallinity, and impurities was used to form a support for reconstruction of BCDI data. Two regions of support were defined: (i) core region with

uniform density constraint and (ii) shell region where the strain was allowed to exhibit non-uniform distribution. Diffraction patterns from (004) and (111) Bragg reflections were first iteratively reconstructed with tight strain and shape constraints and eventually relaxed and combined. Maximum displacement values, deduced from the broadening of the diffraction signals, were set as constraints on the maximum phase difference for the neighboring points in the real space in the final reconstruction.

The final reconstruction of the phase and of the displacement fields are shown in Fig. 9. From the obtained information, authors suggested that the nanowire has the presence of both compressive strains, the core and tensile strain, that develop near the surface. Using the elasticity theory,<sup>21</sup> values of stress were calculated to be about  $-3.6$  GPa in the core region and approaching  $13.4$  GPa near the outermost part of the nanowire. It was suggested that surface impurities and tapering of the nanowire contribute to the non-uniform difference in stress in the volume of the nanowire.

Dynamic study of individual  $400$  nm gold nanoparticle under an applied high pressure was done by Yang *et al.*<sup>58</sup> This

advancement was possible through the use of an optimized sample environment and de-convolution of the mutual coherence function. The application of high pressure *in situ* requires sample environment transparent to X-rays (see Fig. 10). One possible solution is diamond-anvil cells. While this material allows X-rays to pass through without significant distortion, it absorbs a larger portion of the scattered intensity. The authors used a beryllium gasket to preserve the scattered intensity. The distortion of the wave caused by the beryllium gasket was accounted for through the de-convolution of the mutual coherence function. Multiple scans at different pressure and alignment conditions were averaged to reduce the effects of wavefront distortion on reconstructions. The mutual coherence function was reconstructed in the iterative scheme.

With this approach, the authors were able to show that overall strain reduces with increase of pressure while the overall shape undergoes significant changes. They explain this counterintuitive reduction of strain with the isolated nature of the nanoparticle.

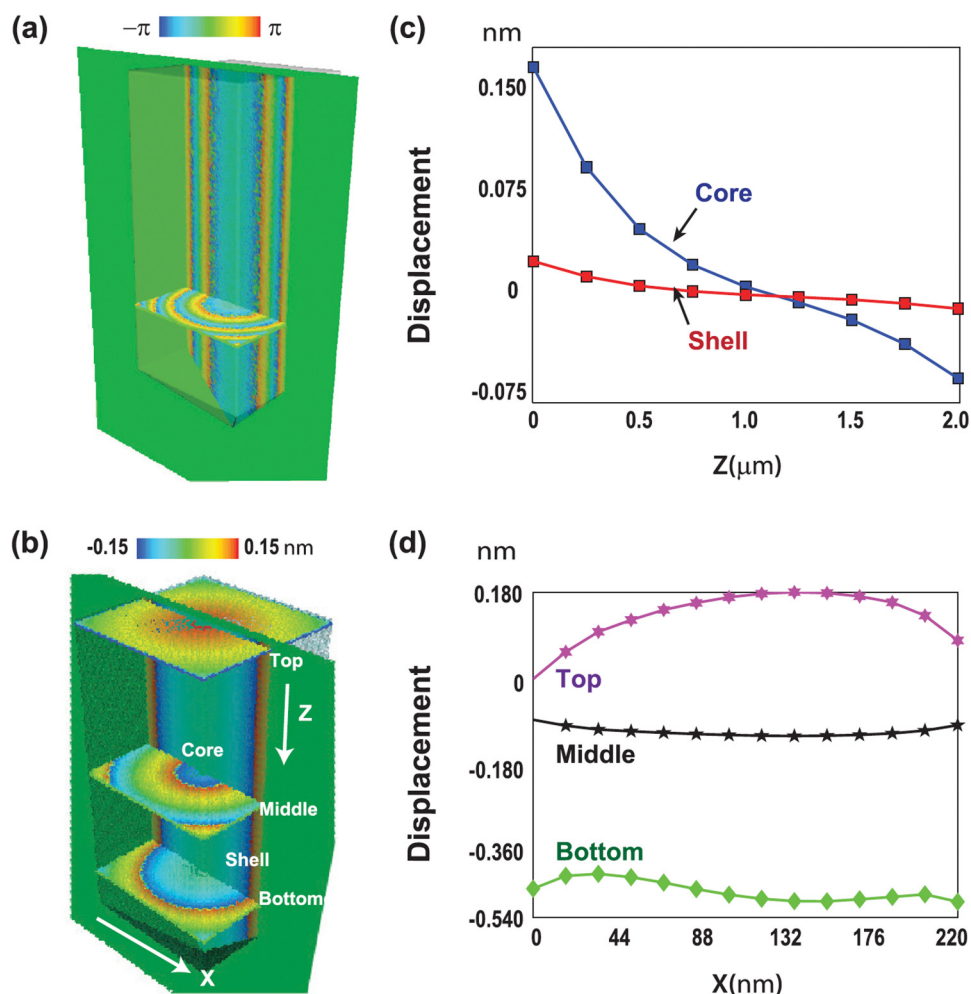


**FIG. 9.** (a) Phase and (b) displacement maps reconstructed for individual Ni nanowire with panels (c) and (d) showing line profiles of the displacement. Reprinted with permission from Fohrtung *et al.* Appl. Phys. Lett. 101, 033107 (2012).<sup>47</sup> Copyright 2012 AIP Publishing LLC.



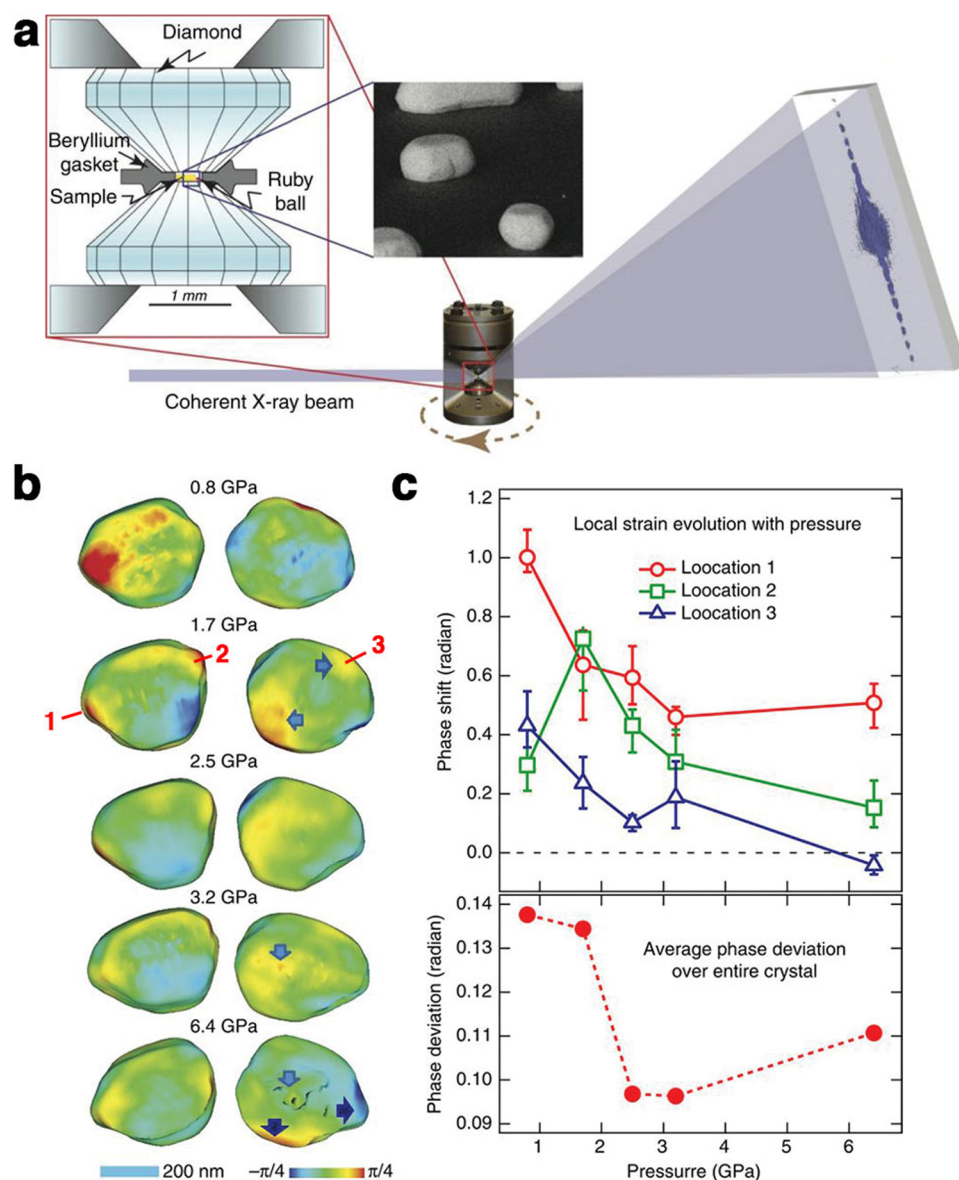


**FIG. 10.** (a) Experimental scheme. (b) Evolution of the phase distribution at different levels of the applied pressure. (c) Phase shifts at different locations marked in (b) and average phase deviation at different pressures. Adapted from Yang *et al.* Nat. Commun. **4**, 1680 (2013).<sup>58</sup> Copyright 2013 Nature Publishing Group.

## B. Semiconductor

The quantification of strain in semiconductors is very important to the charge carrier mobility and bandgap engineering. This quantitative strain knowledge is useful for the generation of CMOS devices and in the emerging world of silicon quantum electronics. A few researchers in academia and industry have utilized Bragg coherent diffractive imaging for this task. Semiconductor materials have been pushed to a scaling-functionality limit over the years, slowly leading to a predicted plateau in famous Moore's law.<sup>59</sup> Freestanding semiconductor nanostructures such as nanowires (NWs) have been broadly studied during the past decade due to their unique electronic, optical, and mechanical properties. A wide

variety of applications based on semiconductor nanostructures have been demonstrated in numerous fields ranging from electronics,<sup>60,61</sup> to photonics,<sup>62–64</sup> photovoltaics,<sup>65,66</sup> and other areas.<sup>67</sup> Engineering strain in semiconductors can help to significantly alter the electronic properties. For instance, the bandgap and charge carrier mobility heavily depend on the strain state of the nanostructure<sup>68,69</sup> that can be tuned during the growth process. Moreover, strain engineering can be also exploited in diluted magnetic semiconductors such as GaMnAs, in which the local strain can affect the easy axis of magnetic anisotropy. Thus, the ability to use the Bragg coherent diffractive imaging to probe strain demonstrates benefits for these studies.

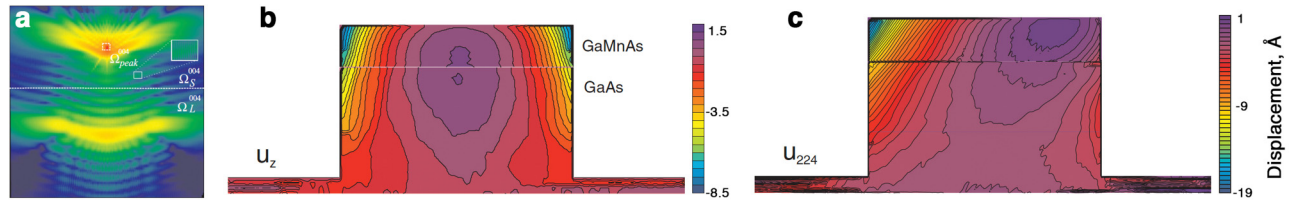


**FIG. 11.** (a) Diffraction pattern near (004) Bragg peak. (b) Vertical component of the displacement vector. (c) Displacement reconstructed from the (224) plane. Adapted from Minkevich *et al.* Phys. Rev. B 84, 054113 (2011).<sup>70</sup> Copyright 2011 American Physical Society.

In Fig. 8, we show an example of experimental results of imaging of the GaMnAs nanostructure.<sup>70</sup> The measured diffraction pattern [see Fig. 11(a)] is the characteristic for a highly strained system which is confirmed by a reconstructed displacement map [see Figs. 11(b)–11(c)]. Horizontal nanowires were fabricated by first growing an epitaxial GaMnAs (of about 0.7% Mn dopant) layer on a GaAs (001) substrate and later lithographically etching it into horizontal periodic nanowires. An interface strain is induced due to the lattice mismatch between two structures (GaMnAs and GaAs) during the growth process. Post growth etching and processing induces an additional strain. The asymmetric, strong diffused cloud and broad centered peaks diffraction pattern [see Fig. 11(a)] indicate a large vertical misfit between the two materials. The vertical extent between the GaAs peak position and that of the GaMnAs peak location scales with the misfit strain along the  $c$ -direction in the material. The directional broadening of both GaAs and GaMnAs peaks also scales with the strain inhomogeneity along the said direction. While the surface roughness could be manifested in the diffused cloud near the Bragg spots. The reconstruction of such data is challenging due to large phase jumps between two structures and can be done by separation of the data in two different regions<sup>70,24</sup> while allowing an alternating support. This approach allows one to obtain two intermediate solutions that can be combined and refined using the whole diffraction data.

In the work by Newton *et al.*<sup>37</sup> six different Bragg reflections from a single ZnO nanowire were recorded (see Fig. 8). With these data, the authors reconstructed three-dimensional displacement

field vector in 3 Cartesian components. The vector was then decomposed into the full strain field tensor as in Eq. (1). The authors showed that 3 orthogonal Bragg reflections are enough for the reconstruction of the displacement field. They also discuss a method for reconstruction of the displacement field from only 2 Bragg reflections.

### C. Perovskite

Perovskites are a class of materials with an  $ABO_3$  principle chemical formula. While sharing a common crystal structure, these materials exhibit a wide range of functional properties from the ferroic domain to superconductivity. These unique properties made them a center of interest in materials science research efforts towards efficient and cheap solar cells, novel functional electronics, high-density memory devices, catalysis, and many other applications.

Manipulating strain in these materials can lead to further improvement of useful properties and, at the nanoscale, plays important role in balancing energies which can play a significant role in the formation of strange textures of polarization, such as ferroelectric vortices.<sup>17</sup> The Bragg coherent diffractive imaging was successfully used not only to image strain in the perovskite barium titanate but also to link it to topological vortices of ferroelectric configuration.<sup>17</sup> Understanding the behavior of ferroelectric domains with relation to strain distribution requires looking at the problem both from an experimental standpoint and from modeling at the nanoscale.

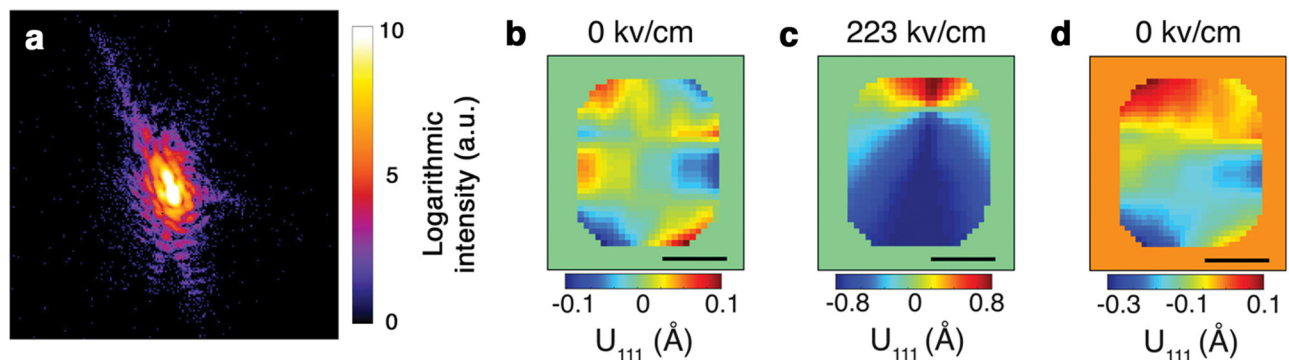


**FIG. 12.** (a) Measured diffraction data. (b)–(d) Reconstructions of the displacement at different electric field levels.<sup>17</sup> Scale bars are 60 nm.

Imaging of ferroelectric domains at the nanoscale using the BCDI technique requires several ingredients, starting with the possibility to manipulate an individual nanoparticles energy landscape with external influences, robust and efficient phase retrieval algorithms capable of reconstructing multiple states of individual nanoparticle in a short time, a metric for the identification of potential nanoparticles with topological textures during the experiment, and a model for the interpretation of the data.

Understanding ferroelectric polarization requires finding its relation to the strain. The spontaneous strain can be related to projections of ferroelectric polarization  $P_k$  and  $P_l$  through the electrostrictive tensor  $Q_{ijkl}$  as follows:<sup>17</sup>

$$\epsilon_{ij}^o = Q_{ijkl} P_k P_l. \quad (20)$$

This allows us to obtain the spatial distribution of ferroelectric polarization from the reconstructed displacement maps. Phase field modeling further allows the interpretation of the results in search of better understanding of the underlying processes in energy landscapes that make it favorable for topologies to emerge or to disappear. The principle equation in the phenomenological approach of Landau relates an order parameter with the evolution of free energy,  $F$ , in the system through the kinetic coefficient,  $L$ ,<sup>17</sup>

$$\frac{\delta P_i(\mathbf{r}, t)}{\delta t} = -L \frac{\delta F}{\delta P_i(\mathbf{r}, t)} \quad (i = 1, 2, 3). \quad (21)$$

Performing modelling of the response of the nanoparticle to an external electric field independently from the reconstructions at the same field levels is important in making an additional check on the quality of the reconstruction. An example of diffraction data and reconstructed slices of the displacement field are shown in Fig. 12. More can be found in Ref. 17.

## V. CONCLUSION

We have discussed the applicability of synchrotron-based X-ray Bragg coherent diffractive imaging (BCDI) to probe, in the real space, nanoscale spatial distributions of strain fields, and their evolution, in a wide class of materials. BCDI has a bright future and is undergoing rapid development (through improvements in experimental techniques, sample environments, and theory) since the first demonstrations about 15 years ago. Strain sensitivity down to the picometer range has been achieved and new materials and exciting science are being actively pursued by a growing number of research groups.

The current resolution of 8–20 nm is expected to further improve by undergoing upgrades of synchrotrons to diffraction limited storage rings. The impervious nature of X-rays to external electric and magnetic fields, temperature, and pressure allows *in operando* and *in situ* studies of electronic, spin, and orbital degrees of freedom in strain engineered materials, which can revolutionize the electronics industry. Real space imaging at the nano- and mesoscales will likely open new perspectives on intermediate states during the transformation of matter, capturing rare events under thermodynamical perturbations.

With these developments, BCDI could potentially become not just a state of the art but a method of choice for academic and

industrial researchers in order to investigate and spatially resolve sub-nanometer atomic behavior in three dimensions, whereas combining BCDI with ultrafast pump-probe techniques may provide unprecedented insights into future physics of strained media.

## ACKNOWLEDGMENTS

This work was supported by the U.S. Department of Defense (DOD) Air Force Office of Scientific Research under Award No. FA9550-18-1-0196 (Program Manager: Dr. Ali Sayir). We also acknowledge support, in part, from the LANSCE Professorship sponsored by the National Security Education Center at LANL under Subcontract No. 257827. This research used resources of the Advanced Photon Source (APS), a U.S. Department of Energy (DOE) Office of Science User Facility operated for the DOE Office of Science by Argonne National Laboratory (ANL) under Contract No. DE-AC02-06CH11357. We also thank the staff at ANL and the APS for their support.

## REFERENCES

- A. D. Caviglia, R. Scherwitzl, P. Popovich, W. Hu, H. Bromberger, R. Singla, M. Mitrano, M. C. Hoffmann, S. Kaiser, P. Zubko, S. Gariglio, J.-M. Triscone, M. Först, and A. Cavalleri, "Ultrafast strain engineering in complex oxide heterostructures," *Phys. Rev. Lett.* **108**, 136801 (2012).
- H. Guo, S. Dong, P. D. Rack, J. D. Budai, C. Beekman, Z. Gai, W. Siemons, C. M. Gonzalez, R. Timilsina, A. T. Wong, A. Herklotz, P. C. Snijders, E. Dagotto, and T. Z. Ward, "Strain doping: Reversible single-axis control of a complex oxide lattice via helium implantation," *Phys. Rev. Lett.* **114**, 256801 (2015).
- M. W. Larsson, J. B. Wagner, M. Wallin, P. Håkansson, L. E. Fröberg, L. Samuelson, and L. R. Wallenberg, "Strain mapping in free-standing heterostructured wurtzite InAs/InP nanowires," *Nanotechnology* **18**, 015504 (2007).
- S. Conesa-Boj, F. Boioli, E. Russo-Averchi, S. Dunand, M. Heiss, D. Rüffer, N. Wyrsch, C. Ballif, L. Miglio, and A. F. i Morral, "Plastic and elastic strain fields in GaAs/Si core-shell nanowires," *Nano Lett.* **14**, 1859–1864 (2014).
- T. F. Kelly and D. J. Larson, "Atom probe tomography 2012," *Annu. Rev. Mater. Res.* **42**, 1–31 (2012).
- H. Franz, O. Leupold, R. Röhlberger, S. V. Roth, O. H. Seeck, J. Spengler, J. Stempf, M. Tischer, J. Viehhaus, E. Weckert, and T. Wroblewski, "Technical report: PETRA III: DESY's new high brilliance third generation synchrotron radiation source," *Synchrotron Radiat. News* **19**, 25–29 (2006).
- J. Feldhaus, J. Arthur, and J. B. Hastings, "X-ray free-electron lasers," *J. Phys. B At. Mol. Opt. Phys.* **38**, 799–819 (2005).
- B. W. J. McNeil and N. R. Thompson, "X-ray free-electron lasers," *Nat. Photonics* **4**, 814–821 (2010).
- F. Döring, A. L. Robisch, C. Eberl, M. Osterhoff, A. Ruhlandt, T. Liese, F. Schlenkrich, S. Hoffmann, M. Bartels, T. Salditt, and H. U. Krebs, "Sub-5 nm hard X-ray point focusing by a combined Kirkpatrick-Baez mirror and multilayer zone plate," *Opt. Exp.* **21**, 19311–19323 (2013).
- A. Schropp, P. Boye, J. M. Feldkamp, R. Hoppe, J. Patommel, D. Samberg, S. Stephan, K. Giewekemeyer, R. N. Wilke, T. Salditt, J. Gulden, A. P. Mancuso, I. A. Vartanyants, E. Weckert, S. Schöder, M. Burghammer, and C. G. Schroer, "Hard X-ray nanobeam characterization by coherent diffraction microscopy," *Appl. Phys. Lett.* **96**, 091102 (2010).
- A. Schropp, R. Hoppe, J. Patommel, D. Samberg, F. Seiboth, S. Stephan, G. Wellenreuther, G. Falkenberg, and C. Schroer, "Hard X-ray scanning microscopy with coherent radiation: Beyond the resolution of conventional X-ray microscopes," *Appl. Phys. Lett.* **100**, 253112 (2012).
- E. Nazaretski, H. Yan, K. Lauer, N. Bouet, X. Huang, W. Xu, J. Zhou, D. Shu, Y. Hwu, and Y. S. Chu, "Design and performance of an X-ray scanning

microscope at the hard X-ray nanoprobe beamline of NSLS-II," *J. Synchrotron Radiat.* **24**, 1113–1119 (2017).

<sup>13</sup>T. Stankevic, D. Dzhigaev, Z. Bi, M. Rose, A. Shabalin, J. Reinhardt, A. Mikkelsen, L. Samuelson, G. Falkenberg, I. A. Vartanyants, and R. Feidenhans'l, "Nanofocused X-ray beams applied for mapping strain in core-shell nanowires," *Proc. SPIE* **9592**, 95920D (2015).

<sup>14</sup>I. K. Robinson, I. A. Vartanyants, G. J. Williams, M. A. Pfeifer, and J. A. Pitney, "Reconstruction of the shapes of gold nanocrystals using coherent X-ray diffraction," *Phys. Rev. Lett.* **87**, 195505 (2001).

<sup>15</sup>G. J. Williams, M. A. Pfeifer, I. A. Vartanyants, and I. K. Robinson, "Three-dimensional imaging of microstructure in Au nanocrystals," *Phys. Rev. Lett.* **90**, 175501 (2003).

<sup>16</sup>H. M. Quiney, G. J. Williams, and E. Fohtung, "Editorial for special issue on coherent diffractive imaging," *J. Opt.* **20**, 010201 (2018).

<sup>17</sup>D. Karpov, Z. Liu, T. dos Santos Rolo, R. Harder, P. V. Balachandran, D. Xue, T. Lookman, and E. Fohtung, "Three-dimensional imaging of vortex structure in a ferroelectric nanoparticle driven by an electric field," *Nat. Commun.* **8**, 280 (2017).

<sup>18</sup>T. Stankevic, D. Dzhigaev, Z. Bi, M. Rose, A. Shabalin, J. Reinhardt, A. Mikkelsen, L. Samuelson, G. Falkenberg, I. A. Vartanyants, and R. Feidenhans'l, "Strain mapping in an InGaN/GaN nanowire using a nanofocused X-ray beam," *Appl. Phys. Lett.* **107**, 103101 (2015).

<sup>19</sup>D. Kriegner, J. Persson, T. Etzelstorfer, D. Jacobsson, J. Wallentin, J. Wagner, K. Deppert, M. Borgström, and J. Stangl, "Structural investigation of GaInP nanowires using X-ray diffraction," *Thin Solid Films* **543**, 100–105 (2013).

<sup>20</sup>V. Favre-Nicolin, J. Eymery, R. Koester, and P. Gentile, "Coherent-diffraction imaging of single nanowires of diameter 95 nanometers," *Phys. Rev. B* **79**, 195401 (2009).

<sup>21</sup>L. D. Landau and E. M. Lifshitz, *Theory of Elasticity* (Pergamon Press, 1970), Vol. 7.

<sup>22</sup>P. Muralt, R. G. Polcawich, and S. Trolier-McKinstry, "Piezoelectric thin films for sensors, actuators, and energy harvesting," *MRS Bull.* **34**, 658–664 (2009).

<sup>23</sup>J. Martín-Sánchez, R. Trotta, A. Mariscal, R. Serna, G. Piredda, S. Stroj, J. Edlinger, C. Schimpf, J. Aberl, and T. Lettner, "Strain-tuning of the optical properties of semiconductor nanomaterials by integration onto piezoelectric actuators," *Semicond. Sci. Technol.* **33**, 013001 (2018).

<sup>24</sup>E. Fohtung, "Strain field and strain engineering in semiconductor nanostructures: Coherent X-ray diffraction imaging and analytical studies," Ph.D. thesis (Fakultät fuer Chemie, Pharmazie und Geowissenschaften, Albert-Ludwigs-Universität Freiburg i. Br., 2010).

<sup>25</sup>L. Mazet, S. M. Yang, S. V. Kalinin, S. Schamm-Chardon, and C. Dubourdieu, "A review of molecular beam epitaxy of ferroelectric BaTiO<sub>3</sub> films on Si, Ge and GaAs substrates and their applications," *Sci. Technol. Adv. Mater.* **16**, 036005 (2015).

<sup>26</sup>T. Zhu and J. Li, "Ultra-strength materials," *Prog. Mater. Sci.* **55**, 710–757 (2010).

<sup>27</sup>A. DeHon, "Array-based architecture for FET-based, nanoscale electronics," *IEEE Trans. Nanotechnol.* **2**, 23–32 (2003).

<sup>28</sup>J. Als-Nielsen and D. McMorrow, *Elements of Modern X-ray Physics* (John Wiley & Sons, Ltd, 2001).

<sup>29</sup>I. A. Vartanyants and I. K. Robinson, "Partial coherence effects on the imaging of small crystals using coherent X-ray diffraction," *J. Phys. Condens. Matter* **13**, 10593 (2001).

<sup>30</sup>I. K. Robinson and I. A. Vartanyants, "Use of coherent X-ray diffraction to map strain fields in nanocrystals," *Appl. Surf. Sci.* **182**, 186–191 (2001).

<sup>31</sup>A. Giacomazzo, *Fundamentals of Crystallography* (Oxford University Press, 2002).

<sup>32</sup>S. Takagi, "Dynamical theory of diffraction applicable to crystals with any kind of small distortion," *Acta Cryst.* **15**, 1311–1312 (1962).

<sup>33</sup>D. Taupin, "Prévision de quelques images de dislocations par transmission des rayons X (cas de Laue symétrique)," *Acta Crystallogr.* **23**, 25–35 (1967).

<sup>34</sup>S. Takagi, "A dynamical theory of diffraction for a distorted crystal," *J. Phys. Soc. Jpn.* **26**, 1239–1253 (1969).

<sup>35</sup>Z. G. Pinsker, *Dynamical Scattering of X-Rays in Crystals, Springer Series in Solid-State Sciences* (Springer-Verlag, Berlin, 1978).

<sup>36</sup>A. Authier, *Dynamical Theory of X-Ray Diffraction, IUCr Monographs on Crystallography* (Oxford University Press, Oxford, 2002).

<sup>37</sup>M. C. Newton, S. J. Leake, R. Harder, and I. K. Robinson, "Three-dimensional imaging of strain in a single ZnO nanorod," *Nat. Mater.* **9**, 120–124 (2010).

<sup>38</sup>I. Robinson and R. Harder, "Coherent X-ray diffraction imaging of strain at the nanoscale," *Nat. Mater.* **8**, 291–298 (2009).

<sup>39</sup>D. Sayre, "Some implications of a theorem due to Shannon," *Acta Crystallogr.* **5**, 843 (1952).

<sup>40</sup>J. R. Fienup, "Phase retrieval algorithms: A comparison," *Appl. Opt.* **21**, 2758–2769 (1982).

<sup>41</sup>J. W. Miao, D. Sayre, and H. N. Chapman, "Phase retrieval from the magnitude of the Fourier transforms of nonperiodic objects," *J. Opt. Soc. Am. A* **15**, 1662–1669 (1998).

<sup>42</sup>S. Marchesini, "Invited article: A unified evaluation of iterative projection algorithms for phase retrieval," *Rev. Sci. Instrum.* **78**, 011301 (2007).

<sup>43</sup>R. W. Gerchberg and W. O. Saxton, "A practical algorithm for the determination of the phase from image and diffraction plane pictures," *Optik* **35**, 237 (1972).

<sup>44</sup>A. Tripathi, "Dichroic coherent diffractive imaging," Ph.D. thesis (Department of Physics, UC San Diego, 2012).

<sup>45</sup>J. Nocedal and S. J. Wright, *Numerical Optimization* (Springer Verlag, New York, 1999).

<sup>46</sup>J. Nocedal, "Updating Quasi-Newton matrices with limited storage," *Math. Comput.* **35**, 773–782 (1980).

<sup>47</sup>E. Fohtung, J. W. Kim, K. T. Chan, R. Harder, E. E. Fullerton, and O. G. Shpyrko, "Probing the three-dimensional strain inhomogeneity and equilibrium elastic properties of single crystal Ni nanowires," *Appl. Phys. Lett.* **101**, 033107 (2012).

<sup>48</sup>J. N. Clark, J. Ihli, A. S. Schenk, Y.-Y. Kim, A. N. Kulak, J. M. Campbell, G. Nisbet, F. C. Meldrum, and I. K. Robinson, "Three-dimensional imaging of dislocation propagation during crystal growth and dissolution," *Nat. Mater.* **14**, 780–784 (2015).

<sup>49</sup>J. N. Clark, L. Beitra, G. Xiong, A. Higginbotham, D. M. Fritz, H. T. Lemke, D. Zhu, M. Chollet, G. J. Williams, M. Messerschmidt, B. Abbey, R. J. Harder, A. M. Korsunsky, J. S. Wark, and I. K. Robinson, "Ultrafast three-dimensional imaging of lattice dynamics in individual gold nanocrystals," *Science* **341**, 56–59 (2013).

<sup>50</sup>A. Ulvestad, A. Singer, J. N. Clark, H. M. Cho, J. W. Kim, R. Harder, J. Maser, Y. S. Meng, and O. G. Shpyrko, "Topological defect dynamics in operando battery nanoparticles," *Science* **348**, 1344–1347 (2015).

<sup>51</sup>D. Attwood and A. Sakdinawat, *X-rays and Extreme Ultraviolet Radiation Principles and Applications* (Cambridge University Press, 2017).

<sup>52</sup>C. Rau, U. Wagner, Z. Pešić, and A. De Fanis, "Coherent imaging at the diamond beamline I13," *Phys. Status Solidi A* **208**, 2522–2525 (2011).

<sup>53</sup>S. J. Leake, V. Favre-Nicolin, E. Zatterin, M.-I. Richard, S. Fernandez, G. Chahine, T. Zhou, P. Boesecke, H. Djazouli, and T. U. Schüll, "Coherent nanoscale X-ray probe for crystal interrogation at ID01, ESRF—the European synchrotron," *Mater. Des.* **119**, 470–471 (2017).

<sup>54</sup>J. Gulden, O. M. Yefanov, A. P. Mancuso, R. Dronyak, A. Singer, V. Bernátová, A. Burkhardt, O. Polozhentsev, A. Soldatov, M. Sprung, and I. A. Vartanyants, "Three-dimensional structure of a single colloidal crystal grain studied by coherent X-ray diffraction," *Opt. Exp.* **20**, 4039–4049 (2012).

<sup>55</sup>U. Johansson, D. Carbone, S. Kalbfleisch, A. Bjorling, A. Rodriguez-Fernandez, T. Stankevic, M. Liebi, B. Bring, A. Mikkelsen, and U. Vogt, "Initial operation of the NanoMAX beamline at MAX IV," *Microsc. Microanal.* **24**(Suppl. 2), 250–251 (2018).

<sup>56</sup>F. Hofmann, E. Tarleton, R. J. Harder, N. W. Phillips, P.-W. Ma, J. N. Clark, I. K. Robinson, B. Abbey, W. Liu, and C. E. Beck, "3D lattice distortions and defect structures in ion-implanted nano-crystals," *Sci. Rep.* **7**, 45993 (2017).

<sup>57</sup>D. Dzhigaev, A. Shabalin, T. Stankevic, U. Lorenz, R. P. Kurta, F. Seiboth, J. Wallentin, A. Singer, S. Lazarev, O. M. Yefanov, M. Borgström, M. N. Strikhanov, L. Samuelson, G. Falkenberg, C. G. Schroer, A. Mikkelsen,



- R. Feidenhans'l, and I. A. Vartanyants, "Bragg coherent X-ray diffractive imaging of a single indium phosphide nanowire," *J. Opt.* **18**, 064007 (2016).
- <sup>58</sup>W. Yang, X. Huang, R. Harder, J. N. Clark, I. K. Robinson, and H.-K. Mao, "Coherent diffraction imaging of nanoscale strain evolution in a single crystal under high pressure," *Nat. Commun.* **4**, 1680 (2013).
- <sup>59</sup>G. E. Moore, "Cramming more components onto integrated circuits," *Electronics* **38**, 114–117 (1965).
- <sup>60</sup>J.-P. Colinge, C.-W. Lee, A. Afzalian, N. Dehdashti Akhavan, R. Yan, I. Ferain, P. Razavi, B. O'Neill, A. Blake, M. White, A.-M. Kelleher, B. McCarthy, and R. Murphy, "Nanowire transistors without junctions," *Nat. Nanotechnol.* **5**, 225–229 (2010).
- <sup>61</sup>S. Ju, A. Facchetti, Y. Xuan, J. Liu, F. Ishikawa, P. Ye, C. Zhou, T. J. Marks, and D. B. Janes, "Fabrication of fully transparent nanowire transistors for transparent and flexible electronics," *Nat. Nanotechnol.* **2**, 378–384 (2007).
- <sup>62</sup>C. Y. Chen, G. Zhu, Y. Hu, J. W. Yu, J. Song, K. Y. Cheng, L. H. Peng, L. J. Chou, and Z. L. Wang, "Gallium nitride nanowire based nanogenerators and light-emitting diodes," *ACS Nano* **6**, 5687–5692 (2012).
- <sup>63</sup>F. Qian, S. Gradecak, Y. Li, C. Y. Wen, and C. M. Lieber, "Core/multishell Nanowire heterostructures as multicolor, high-efficiency light-emitting diodes," *Nano Lett.* **5**, 2287–2291 (2005).
- <sup>64</sup>R. Yan, D. Gargas, and P. Yang, "Nanowire photonics," *Nat. Photonics* **3**, 569–576 (2009).
- <sup>65</sup>P. Krogstrup, H. I. Jørgensen, M. Heiss, O. Demichel, J. V. Holm, M. Aagesen, J. Nygard, and A. F. I. Morral, "Single-nanowire solar cells beyond the Shockley–Queisser limit," *Nat. Photonics* **7**, 306–310 (2013).
- <sup>66</sup>J. Wallentin, N. Anttu, D. Asoli, M. Huffman, I. Aberg, M. H. Magnusson, G. Siefert, P. Fuss-Kailuweit, F. Dimroth, B. Witzigmann, H. Q. Xu, L. Samuelson, K. Deppert, and M. T. Borgström, "Inp nanowire array solar cells achieving 13.8% efficiency by exceeding the ray optics limit," *Science* **339**, 1057–1060 (2013).
- <sup>67</sup>N. P. Dasgupta, J. Sun, C. Liu, S. Brittman, S. C. Andrews, J. Lim, H. Gao, R. Yan, and P. Yang, "25th anniversary article: Semiconductor nanowires—synthesis, characterization, and applications," *Adv. Mater.* **26**, 2137–2184 (2014).
- <sup>68</sup>K. J. Kuhn, "Moore's crystal ball: Device physics and technology past the 15 nm generation," *Microelectron. Eng.* **88**, 1044–1049 (2011).
- <sup>69</sup>M. Montazeri, M. Fickenscher, L. M. Smith, H. E. Jackson, J. Yarrison-Rice, J. H. Kang, Q. Gao, H. Hoe Tan, C. Jagadish, Y. Guo, J. Zou, M.-E. Pistol, and C. E. Pryor, "Direct measure of strain and electronic structure in GaAs/GaP core–shell nanowires," *Nano Lett.* **10**, 880–886 (2010).
- <sup>70</sup>A. A. Minkevich, E. Fohtung, T. Slobodskyy, M. Riotte, D. Grigoriev, M. Schmidbauer, A. C. Irvine, V. Novak, V. Holy, and T. Baumbach, "Selective coherent X-ray diffractive imaging of displacement fields in (Ga,Mn)As/GaAs periodic wires," *Phys. Rev. B* **84**, 054113 (2011).